Non-Stoichiometric Redox Active Perovskite Materials for Solar Thermochemical Fuel Production: A Review

Anita Haeussler, Stéphane Abanades, Julien Jouannaux, Anne Julbe

catalysts

MDPI

Review

Non-Stoichiometric Redox Active Perovskite Materials for Solar Thermochemical Fuel Production: A Review

Anita Haeussler [1], Stéphane Abanades [1,*], Julien Jouannaux [2] and Anne Julbe [2]

[1] Processes, Materials and Solar Energy Laboratory, CNRS-PROMES, 7 Rue du Four Solaire, 66120 Font-Romeu, France; anita.haeussler@promes.cnrs.fr

[2] Institut Européen des Membranes, IEM, UMR-5635, Université de Montpellier, ENSCM, CNRS, 2 Place Eugène Bataillon, CEDEX 5, 34095 Montpellier, France; julien.jouannaux@umontpellier.fr (J.J.); anne.julbe@umontpellier.fr (A.J.)

* Correspondence: stephane.abanades@promes.cnrs.fr; Tel.: +33-046-830-7730

Received: 5 November 2018; Accepted: 22 November 2018; Published: 3 December 2018

Abstract: Due to the requirement to develop carbon-free energy, solar energy conversion into chemical energy carriers is a promising solution. Thermochemical fuel production cycles are particularly interesting because they can convert carbon dioxide or water into CO or H_2 with concentrated solar energy as a high-temperature process heat source. This process further valorizes and upgrades carbon dioxide into valuable and storable fuels. Development of redox active catalysts is the key challenge for the success of thermochemical cycles for solar-driven H_2O and CO_2 splitting. Ultimately, the achievement of economically viable solar fuel production relies on increasing the attainable solar-to-fuel energy conversion efficiency. This necessitates the discovery of novel redox-active and thermally-stable materials able to split H_2O and CO_2 with both high-fuel productivities and chemical conversion rates. Perovskites have recently emerged as promising reactive materials for this application as they feature high non-stoichiometric oxygen exchange capacities and diffusion rates while maintaining their crystallographic structure during cycling over a wide range of operating conditions and reduction extents. This paper provides an overview of the best performing perovskite formulations considered in recent studies, with special focus on their non-stoichiometry extent, their ability to produce solar fuel with high yield and performance stability, and the different methods developed to study the reaction kinetics.

Keywords: perovskites; oxygen vacancies; non-stoichiometric materials; thermochemical cycles; CO_2/H_2O splitting; hydrogen; solar fuel; concentrating solar technologies

1. Introduction

World energy requirements are still increasing, and fossil fuels combustion contributes to global warming. Currently, most of the world energy production comes from fossil fuels and nuclear. Fossil fuels are limited resources and their combustion produces carbon dioxide which contributes to the greenhouse effect. By contrast, nuclear energy does not produce CO_2 but radioactive waste whose treatment is very expensive [1]. In this context, solar energy is a valuable solution as it is free, inexhaustible, and does not produce CO_2 emissions. However, solar energy is intermittent, variable, and diffuse. With this in mind, thermochemical cycles using concentrated solar energy permit to convert solar energy into chemical fuels, which can be used on demand, stored, and transported. Thermochemical cycles based on metal oxides encompass two steps. First, a solar-activated thermal reduction (TR) of the material at high temperature creates oxygen vacancies in the oxide lattice, producing O_2, as represented by the reaction (1). Concentrated solar energy can be used as the

external source of high temperature heat to drive the reaction. The second step is an exothermic reaction, in which the material is re-oxidized by H_2O or CO_2, represented by the reactions (2a) and (2b), respectively. The hydrogen product can be directly used as a fuel (e.g., in fuel cells), whereas syngas (mixture of H_2/CO) can be converted into synthetic liquid hydrocarbon fuels via the Fischer–Tropsch process [2]. The metal oxide is not consumed in the overall H_2O and CO_2 splitting process, and thus, acts as a catalyst in the global reaction.

$$M_xO_y \rightarrow M_xO_{y-\delta} + \frac{\delta}{2}O_2 \quad (1)$$

$$M_xO_{y-\delta} + \delta H_2O \rightarrow M_xO_y + \delta H_2 \quad (2a)$$

$$M_xO_{y-\delta} + \delta CO_2 \rightarrow M_xO_y + \delta CO \quad (2b)$$

However, thermochemical cycles currently exhibit low efficiency which prevents commercial use in the short term. To date, the highest solar-to-fuel energy conversion efficiency has reached 5% for ceria reticulated porous foam [3], while the efficiency should at least be of 20% to permit industrialization and to compete with photovoltaic technology combined with electrolysis [4]. In the aim of increasing the efficiency, both the solar reactor thermal efficiency and the material fuel productivity can be improved. Improving the overall process efficiency requires increasing the fuel production yields and rates while decreasing the operating temperature to reduce heat losses. In addition, the reactive materials used in thermochemical cycles should be thermally-stable in order to keep a stable production over repeated redox cycles. Among the investigated candidate materials, ceria has been extensively studied for thermochemical cycles due to several desirable thermodynamic and physico-chemical properties. Ceria (CeO_2) is able to maintain its crystal structure over a large range of non-stoichiometry and operating conditions. It exhibits rapid reaction kinetics and fast oxygen diffusion rates, which promotes the reversible phase transitions between the oxidized and partially reduced states in a large range of non-stoichiometry. However, it requires a high reduction temperature to produce substantial reduction extent due to high enthalpy change. The high reduction temperature induces sintering and reactor materials issues, and thus limits the practical use of ceria. Different dopants were investigated to increase fuel production while lowering the reduction temperature, like Li^{2+}, Mg^{2+}, Sc^{3+}, Dy^{3+}, La^{3+}, Sm^{3+}, Gd^{3+}, Pr^{3+}, Hf^{4+}, and Zr^{4+} [5–14], at the expense of lowering the oxidation rate. In spite of the numerous dopants investigated, the relatively low fuel productivity of ceria still limits its future implementation in large-scale processes [5]. Recently, perovskite-structured materials have emerged as promising candidate catalysts for high-temperature thermochemical fuel production [6]. Highly reducible and thermally-stable perovskites with high oxygen exchange and transport properties have been proposed [15–17]. The theoretical materials performance is ruled by thermodynamics, but in reality, another limitation to the final fuel production achieved is related to reaction kinetics. In this paper, the first section describes the redox system thermodynamics, then the perovskite formulations that were studied in thermochemical cycles are summarized, and finally the methods used to study the perovskites redox reaction kinetics are described.

2. Thermodynamics of Thermochemical Cycles

Investigating perovskite thermodynamics allows predicting the theoretical maximum fuel production that can be reached in thermochemical cycles, as a function of reduction and oxidation temperatures and partial pressure of oxygen. In order to achieve spontaneous reactions, it is required to satisfy criteria (3) and (4), where ΔG° represents the standard Gibbs free enthalpy variation, P_{O_2} the oxygen partial pressure, T the temperature, and the subscripts *TR*, *WS*, and *CDS* refer to the thermal reduction, the water splitting, and the carbon dioxide splitting, respectively [16]. The Figure 1 represents the Gibbs free energy in standard conditions for CO_2 splitting and for $La_{0.6}Sr_{0.4}MnO_3$ during the reduction and oxidation steps. The Gibbs free energy of the reduction reaction is computed with values of ΔH° and ΔS° found in the literature [18]. Concerning the CO_2 splitting, its Gibbs free

energy comes from the thermochemical database of HSC chemistry software. The Gibbs free energy of oxidation corresponds to the difference between the Gibbs free energies of CO_2 splitting and of $La_{0.6}Sr_{0.4}MnO_3$ reduction. It can be seen that the thermal reduction is favorable for temperature higher than T_{high} and the oxidation step is promoted for temperature lower than T_{low} [8].

$$\Delta G^{\circ}{}_{TR}\left(P_{O_2,TR},\ T_{TR}\right) < 0 \tag{3}$$

$$\Delta G^{\circ}{}_{WS}\left(P_{O_2,WS},\ T_{WS}\right) < -\Delta G^{\circ}{}_{H_2O}\left(P_{O_2,WS},\ T_{WS}\right) \tag{4a}$$

$$\Delta G^{\circ}{}_{CDS}\left(P_{O_2,CDS},\ T_{CDS}\right) < -\Delta G^{\circ}{}_{CO_2}\left(P_{O_2,CDS},\ T_{CDS}\right) \tag{4b}$$

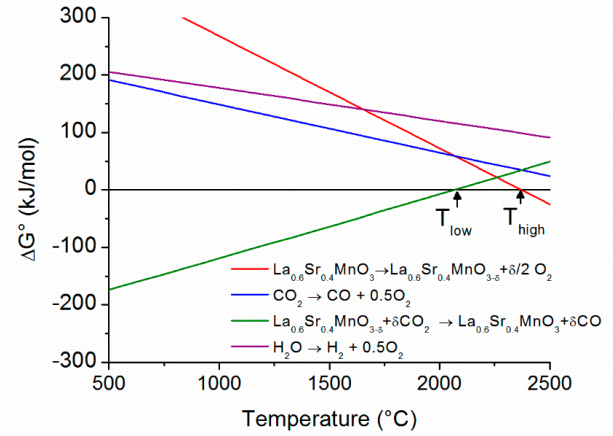

Figure 1. Schematic plot of the Gibbs energy for carbon dioxide splitting, water splitting, and two-step thermochemical redox cycling of $La_{0.6}Sr_{0.4}MnO_3$ in standard conditions.

The Gibbs energy variation for the reduction and the oxidation steps are defined by Equations (5) and (6), respectively, whereas Equations (7) and (8) define the enthalpy and entropy variation of the overall cycle;

$$\Delta G^{\circ}{}_{TR,\,T_{TR}} = \Delta H^{\circ}{}_{red} - T_{TR}\left(\Delta S^{\circ}{}_{red} + \frac{1}{2}S^{O_2}_{T_{TR}}\right) \tag{5}$$

$$\Delta G^{\circ}{}_{WS,\,T_{WS}} = -\Delta H^{\circ}{}_{red} - \Delta H^{H_2O}_{f,\,T_{WS}} - T_{WS}\left(S^{H_2}_{T_{WS}} - S^{H_2O}_{T_{WS}} - \Delta S^{\circ}{}_{red}\right) \tag{6a}$$

$$\Delta G^{\circ}{}_{CDS,\,T_{CDS}} = -\Delta H^{\circ}{}_{red} - \Delta H^{CO_2}_{f,\,T_{CDS}} + \Delta H^{CO}_{f,\,T_{CDS}} - T_{CDS}\left(S^{CO}_{T_{CDS}} - S^{CO_2}_{T_{CDS}} - \Delta S^{\circ}{}_{red}\right) \tag{6b}$$

$$\Delta H^{\circ}{}_{cycle} = \Delta H^{\circ}{}_{TR} + \Delta H^{\circ}{}_{WS} \tag{7}$$

$$\Delta S^{\circ}{}_{cycle} = \Delta S^{\circ}{}_{TR} + \Delta S^{\circ}{}_{WS} \tag{8}$$

where ΔH and ΔS correspond to the standard enthalpy and entropy variation, T_i is the temperature during the WS or TR reaction. From the Equation (6), the oxidation step is exothermic because the oxidation step is entropically unfavorable and the two steps have to be exergonic. Due to $\Delta H_{WS} < 0$, ΔH_{TR} has to be at least higher than ΔH_{CO_2} in order to have $\Delta H_{cycle} > \Delta H_{CO_2}$ [19–21]. At non-standard pressures, the effect of oxygen partial pressure on the entropy variation can be expressed as Equation (9), where P° is the reference pressure:

$$\Delta S_{TR} = \Delta S^{\circ}{}_{TR} - \frac{1}{2}R\ln\left(\frac{P_{O_2}}{P^{\circ}}\right) \tag{9}$$

The enthalpy variation can be considered as pressure-independent, which conducts to express the Gibbs free enthalpy variation in non-standard pressures, as Equation (10) [22].

$$\Delta G_{TR} = \Delta H^{\circ}{}_{TR} - T\Delta S^{\circ}{}_{TR} + \frac{1}{2}RT\ln\left(\frac{P_{O_2}}{P^{\circ}}\right) \tag{10}$$

When the reduction step is at equilibrium, the Gibbs free enthalpy is nil which allows writing the Equation (5) in the form of Equation (11) for a given value of δ.

$$\ln\left(\frac{p_{O_2}}{p^\circ}\right) = \frac{2\Delta S_{red}}{R} - \frac{2\Delta H_{red}}{RT}\bigg|_{\delta=constant} \quad (11)$$

The oxygen non-stoichiometry is plotted in Figure 2 as a function of the logarithm of the oxygen partial pressure at different temperatures. Then, it is possible to plot the logarithm of the oxygen partial pressure as a function of the inverse of temperature for a constant δ value, and to determine both ΔH_{red} and ΔS_{red} via Equation (11) [6]. For the oxidation step, the contribution of the amount of oxidant gas can be expressed as in Equation (12), where P_{CO}, P_{CO_2} P_{H_2} and P_{H_2O} are the carbon monoxide, carbon dioxide, hydrogen and steam partial pressure, respectively [22]. From Equation (12), it can be evidenced that the increase of the oxidant gas ratio tends to decrease ΔG_{WS} which favors the oxidation reaction. However, increasing the oxidant gas in excess amount may negatively impact the thermochemical cycle efficiency, due to the low conversion yield of the oxidant gas to the splitting products.

$$\Delta G_{WS} = \Delta H^\circ{}_{WS} - T\Delta S^\circ{}_{WS} + RT\ln\left(\frac{P_{H_2}}{P_{H_2O}}\right) \quad (12a)$$

$$\Delta G_{CDS} = \Delta H^\circ{}_{CDS} - T\Delta S^\circ{}_{CDS} + RT\ln\left(\frac{P_{CO}}{P_{CO_2}}\right) \quad (12b)$$

Thus, an ideal redox material must have a low enthalpy variation $\Delta H^\circ{}_{red}$ which permits to increase the reduction extent at a lower temperature. In contrast, a high entropy variation $\Delta S^\circ{}_{red}$ is required, thereby allowing smaller temperature variation between the reduction and the re-oxidation steps, which is critical for overall efficiency [6]. The Gibbs free enthalpy variation can be adjusted by changing the operating conditions (lower oxygen partial pressure or oxidant excess) but this induces energy penalty.

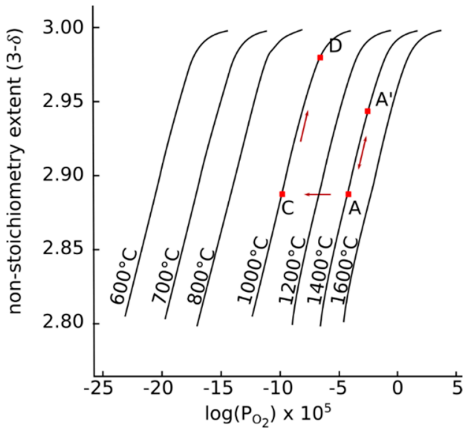

Figure 2. Oxygen non-stoichiometry of $La_{0.6}Sr_{0.4}MnO_3$ as a function of the logarithm of oxygen partial pressure at different temperatures (adapted from Reference [23]). Pressure-swing vs. temperature-swing thermochemical pathways: isothermal cycle at 1400 °C with pressure swing operation between **A** and **A'**, two-temperature cycling with quenching (**A** to **C**), oxidation at 1000 °C (**C** to **D**) and reduction at 1400 °C (**D** to **A**) [24].

3. Perovskite Formulations Investigated for Thermochemical Cycles

Since a few years ago, perovskites have been investigated for solar fuel production from thermochemical cycles [25]. Perovskites have the general formula ABO_3, where A and B are cations. The A cation is 12-fold coordinated with oxygen and it is larger than the B cation. The latter is 6-fold coordinated with oxygen anion. Ideal perovskites present a cubic structure with space group Pm3m,

as represented in Figure 3 [26]. Different elements can occupy the A and B sites of the perovskite according to their ionic radius. The ionic radius of the A cation is comprised between 1.10 and 1.80 Å, whereas the ionic radius of the B cation is comprised between 0.62 and 1.00 Å [17]. The Goldschmidt tolerance factor (Equation (13)) determines whether the perovskite structure can be formed according to the ionic radii. In this equation, r_A, r_B, and r_O are the ionic radii of cation A, cation B, and oxygen anion, respectively. This factor has to be close to one, so that the perovskite can be formed and equals one in the case of an ideal perovskite structure. Rhombohedral perovskites can be formed if t is approximately greater than 1.02. Orthorhombic and tetragonal perovskites can be formed if $t < 1$.

$$t = \frac{r_A + r_O}{\sqrt{2}(r_B + r_O)} \quad (13)$$

The large non-stoichiometry of perovskites is a very interesting property for thermochemical cycles [27]. Due to the large number of dopant insertion options (27 possibilities for the A site and 35 possibilities for the B site), their composition can be tuned to optimize fuel production [28,29].

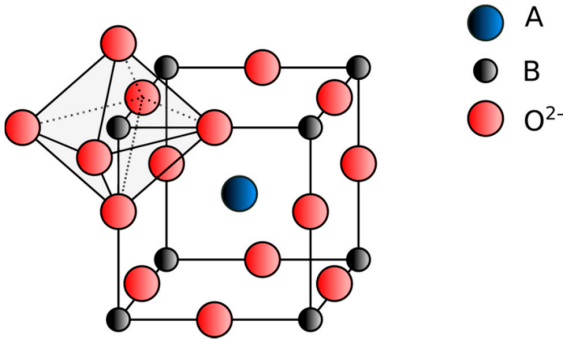

Figure 3. Ideal cubic perovskite structure with an octahedral site.

3.1. Lanthanum–Manganite Perovskites

3.1.1. A-Site Substituted Materials

Among the lanthanum–manganese perovskites series, the most studied is $La_{1-x}Sr_xMnO_3$. $LaMnO_3$ presents a very low reduction extent, which prevents the fuel production. The presence of Sr in the A-site increases the oxidation state of Mn, due to the lower charge of Sr^{2+} compared to La^{3+}. The increase of Mn oxidation state permits to increase the reduction extent. The reduction extent thus increases with the Sr content [23,30–36]. In the same conditions, 24 µmol/g of O_2 are produced for x = 0.1 versus 215 µmol/g of O_2 for x = 0.4. The optimum content for Sr substituting La is comprised between 0.3 and 0. [23,30–32]. The increase of Sr content adversely affects the re-oxidation yield. Demont and Abanades reported a re-oxidation yield of 92% with 35% Sr content, decreasing to 14% with 80% Sr content (at T_{red} = 1400 °C and T_{ox} = 1050 °C) [37]. The Figure 4 represents the CO production for different Sr contents in $La_{1-x}Sr_xMnO_3$, and for undoped and Zr-doped CeO_2 as reference materials. All the $La_{1-x}Sr_xMnO_3$ perovskites present a higher CO production than pure ceria during cycles. $La_{0.5}Sr_{0.5}MnO_3$ presents the highest CO production and can compete with $(Ce,Zr)O_2$ [38]. The use of Sr as dopant in the A-site has also an impact on the grain morphology. A low Sr content favors particle agglomeration whereas crystals have sharp edges with high Sr content [39]. The grain size tends to decrease with the increase of Sr content [30,39]. From a kinetic point of view, the characteristic time, defined as the time required to reach 10% of the peak production rate, is not affected by the Sr content during the reduction step. On the contrary, the characteristic time is strongly increased by the increase of Sr content during the oxidation step [30].

The Ca^{2+} cation can also be used to substitute lanthanum. $La_{1-x}Ca_xMnO_3$ has a lower lattice parameter than $La_{1-x}Sr_xMnO_3$ due to the lower Ca^{2+} ionic radius ($r_{Ca^{2+}} = 1.34$ A) than

Sr^{2+} ($r_{Sr^{2+}} = 1.58\ A$) [40]. The increase of Ca content decreases the lattice parameter due to the increase of the Mn ionic radius induced by the change in the oxidation state. Similarly, to the Sr dopant, Ca permits to increase the reduction extent. Furthermore, this increase is more pronounced than with Sr, because of the larger decrease of the Gibbs' free enthalpy [41–44]. This can be attributed to the smaller ionic radius of Ca^{2+} compared to Sr^{2+} [18,45–47]. The substitution of lanthanum by calcium also permits to diminish the reduction temperature [48]. However, a decrease of the re-oxidation yield is reported by Demont and Abanades: substituting La with 35% of Ca results in a re-oxidation yield of 63% which falls to 33% in the same conditions when the amount of Ca is 50% [41]. Furthermore, the CO production is lower when Ca is used as dopant (210 µmol/g) instead of Sr (269 µmol/g) [41,49]. This can be explained by a larger standard Gibbs free enthalpy [41]. In addition, $La_{1-x}Ca_xMnO_3$ seems more sensitive to the sintering than $La_{1-x}Sr_xMnO_3$, which can have a negative impact on the oxidation step [50].

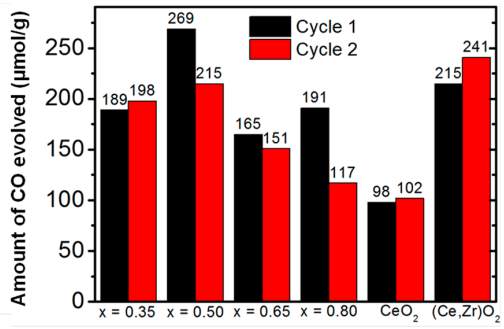

Figure 4. CO production at 1050 °C (with T_{red} = 1400 °C) for the $La_{1-x}Sr_xMnO_3$ series and fluorite materials as referenced during two cycles [38].

Another possible dopant for the A-site in the lanthanum–manganese perovskites is Ba^{2+}, leading to the $La_{1-x}Ba_xMnO_3$ series. The lattice parameter is higher than for $La_{1-x}Sr_xMnO_3$ perovskite, due to a higher ionic radius of Ba^{2+} ($r_{Ba^{2+}} = 1.61\ A$) compared to Sr^{2+} ($r_{Sr^{2+}} = 1.44\ A$). The presence of Ba^{2+} does not show any benefic effect on the reduction extent when compared with Sr and Ca dopants. For instance, an O_2 production of 203 µmol/g was measured for $La_{0.5}Ba_{0.5}MnO_3$, while Sr and Ca containing materials produced 248 µmol/g and 311 µmol/g, respectively (Figure 5). Another point is that the re-oxidation yield is also reduced compared with Sr or Ca-doped lanthanum–manganese perovskites [41].

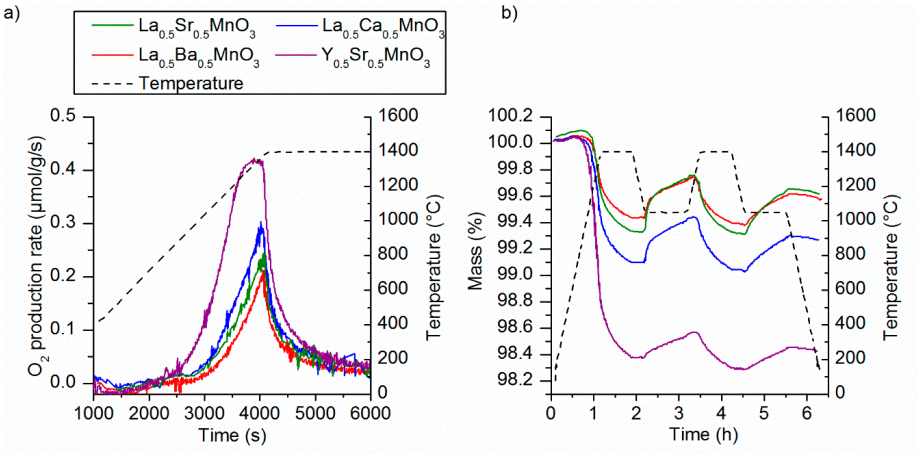

Figure 5. (**a**) O_2 production rates derived from thermogravimetric analysis (TGA) data for $La_{0.5}Ca_{0.5}MnO_3$, $La_{0.5}Ba_{0.5}MnO_3$, $Y_{0.5}Sr_{0.5}MnO_3$, and $La_{0.5}Sr_{0.5}MnO_3$, (**b**) TGA of the same materials during reduction at 1400 °C under Ar, followed by oxidation with CO_2 at 1050 °C (two cycles) [41].

3.1.2. B-Site Substituted Materials

As shown previously, lanthanum–manganese perovskites do not show complete re-oxidation. In order to improve the re-oxidation yield, the B-site was doped with aluminum element. The presence of Al also permits to increase the reduction extent [18,41,45,50–52] In the case of (La,Sr)MnO_3 perovskites, the presence of Al^{3+} cation in the B-site permits to increase the reaction kinetics. The introduction of Al^{3+} in the structure leads to strong atomic interaction due to the decrease of the unit cell volume, which leads to a better stability. Nevertheless, it also diminishes the amount of Mn cation, thus reducing the redox capacity [53]. In addition, reduction of $La_{1-x}Sr_xMn_{1-y}Al_yO_3$ has an onset temperature 300 °C, lower than CeO_2 revealing a lower reduction enthalpy, which promotes the reduction extent [51]. The presence of Al^{3+} enables the reduction of Mn^{4+} to Mn^{3+} but prevents the reduction of Mn^{3+} to Mn^{2+} [54]. The enthalpy variation of $La_{0.2}Sr_{0.8}Mn_{0.8}Al_{0.2}O_3$ and $La_{0.4}Sr_{0.6}Mn_{0.8}Al_{0.2}O_3$ decreases when increasing the δ, as shown by Ezbiri et al. [55]. McDaniel et al. [51] performed 80 cycles with $La_{0.6}Sr_{0.4}Mn_{0.6}Al_{0.4}O_3$ and they obtained a constant CO production, proving that the material was not deactivated. Deml et al. [56] studied the oxygen vacancy formation energy (E_V) of 18 perovskites from $La_{1-x}Sr_xMn_{1-y}Al_yO_3$ series. They highlighted that the E_V decreases with the Sr ratio increase and it increases or stays nearly constant with the Mn ratio increase. It was also shown that $La_{1-x}Sr_xMn_{1-y}Al_yO_3$ has a large range of E_V, from 0 to more than 3 eV, which promotes the vacancy formation, thus the redox activity. The optimal range of E_V for reduction and oxidation reaction is: 1.8 eV $< E_V <$ 2.4 eV (with experimental conditions used by McDaniel et al. [51]). The reduction is promoted by $E_V <$ 2.4 eV whereas the oxidation is promoted by $E_V >$ 1.8 eV [56]. Deml et al. [56] studied three perovskites ($La_{0.6}Sr_{0.4}Mn_{0.6}Al_{0.4}O_3$; $La_{0.4}Sr_{0.6}Mn_{0.6}Al_{0.4}O_3$; and $La_{0.6}Sr_{0.4}Mn_{0.4}Al_{0.6}O_3$) that were selected by McDaniel et al. [51] for their ability to be used in thermochemical cycles. These perovskites have a predicted E_V (2.6, 1.4, and 2.2 ± 0.2 eV, respectively) that corresponds to a favorable reduction. Furthermore, $La_{0.6}Sr_{0.4}Mn_{0.6}Al_{0.4}O_3$ and $La_{0.6}Sr_{0.4}Mn_{0.4}Al_{0.6}O_3$ have a predicted E_V > 1.8 that promotes oxidation. However, $La_{0.4}Sr_{0.6}Mn_{0.6}Al_{0.4}O_3$ produces less H_2 than $La_{0.6}Sr_{0.4}Mn_{0.6}Al_{0.4}O_3$ whose E_V < 1.8, this is due to lower oxidation yield caused by the lower E_V of $La_{0.4}Sr_{0.6}Mn_{0.6}Al_{0.4}O_3$. Finally, Deml et al. [56] presented $La_{0.6}Sr_{0.4}Mn_{0.6}Al_{0.4}O_3$ as the optimal composition for thermochemical cycles. In an experimental study using the same material composition, the fuel production was not stable and the re-oxidation yield dropped from 57% to 35% between the first and second cycle for $La_{0.6}Sr_{0.4}Mn_{0.4}Al_{0.6}O_3$ [41]. A low H_2 production for this material was also highlighted by Sugiyama et al. [57]. Furthermore, Nair and Abanades [49]. found that the use of Al did not improve the reactivity compared to $La_{1-x}Sr_xMnO_3$ perovskites The Al^{3+} cation was also used as B-site dopant in $La_{1-x}Ca_xMnO_3$. Takacs et al. [18] found that the O_2 production of $La_{1-x}Ca_xMn_{1-y}Al_yO_3$ was superior to the one of $La_{1-x}Ca_xMnO_3$ and $La_{1-x}Sr_xMn_{1-y}Al_yO_3$. However, the oxidation temperature must be lower than 850 °C for a complete re-oxidation, which induces energy penalty due to the necessity to reheat the material [50]. The optimal composition was found to be $La_{0.6}Ca_{0.4}Mn_{0.6}Al_{0.4}O_3$ which produces more hydrogen (429 µmol/g) than ceria (56 µmol/g) in similar experimental conditions (reduction at 1400 °C, oxidation at 1000 °C) [58]. For both $La_{1-x}Ca_xMnO_3$ and $La_{1-x}Sr_xMnO_3$ with Al dopant on the B-site, it was also proved that the presence of the dopant in the B-site avoids the carbonate formation at low temperature during the carbon dioxide splitting [39].

Gallium was also considered as B-site dopant in $La_{1-x}Ca_xMnO_3$. The introduction of Ga^{3+} allowed increasing O_2 and CO production. The $La_{0.6}Ca_{0.4}Mn_{0.8}Ga_{0.2}O_3$ perovskite produced 212 µmol/g of O_2, while the undoped perovskite produced only 167 µmol/g (at T_{red} = 1300 °C). During the oxidation step at 900 °C, the Ga-doped perovskite produced 401 µmol/g of H_2 whereas the undoped perovskite produced 339 µmol/g. The fuel production was promoted by the high specific surface area of the perovskite, as it favors solid—gas interactions. However, the substitution of Mn by Ga was limited to 30% in the Sr-doped lanthanum–manganese perovskite [59].

The beneficial effect of the Mg^{2+} cation as dopant in the B-site of $La_{1-x}Sr_xMnO_3$ was also highlighted [41]. Mg^{2+} does not participate to the redox reactions, but it improves the resistance

to sintering and the thermal stability. It can be noticed in Figure 6 that during the first cycle $La_{0.6}Sr_{0.4}Mn_{0.4}Al_{0.6}O_3$ produced the highest CO amount while $La_{0.6}Sr_{0.4}Mn_{0.83}Mg_{0.17}O_3$ kept the highest CO production during the second cycle, showing a stable fuel production upon two cycles (209 and 207 µmol/g, respectively). Furthermore, the use of Mg permits to reduce grain growth during cycles and to obtain smaller grain size compared to the undoped perovskite. Smaller grain sizes induce higher specific surface areas, and thus, promotes the oxidation step. Notwithstanding this effect, the use of Mg dopant is limited to ~15–20% due to its low solubility [41].

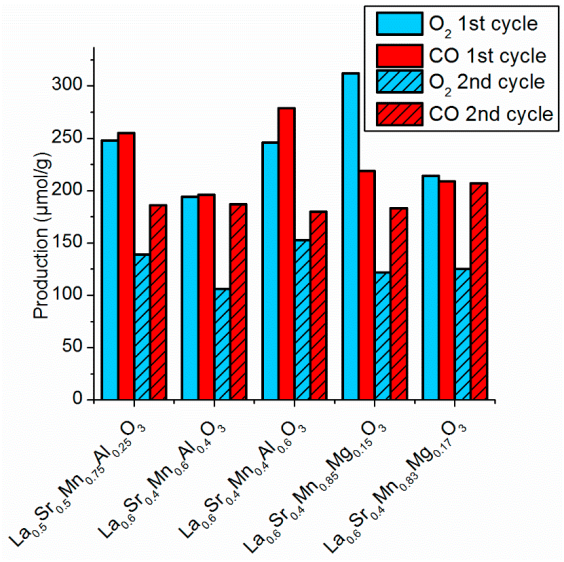

Figure 6. Comparison of O_2 and CO production for $La_{1-x}Sr_xMn_{1-y}Al_yO_3$ and $La_{1-x}Sr_xMn_{1-y}Mg_yO_3$ perovskite series (T_{red} = 1400 °C and T_{ox} = 1050 °C) [41].

Scandium was also considered as B-site dopant in Sr-doped lanthanum–manganese perovskite, but its content was limited to 10% due to its low solubility. Despite this, the introduction of only 5% of Sc increases the O_2 production by a factor of two when compared with $La_{0.5}Sr_{0.5}MnO_3$, according to Dey et al. [60]. However, the authors also present an almost full and very fast re-oxidation whatever the investigated materials, which may be due to flaws in the experimental procedure given that the re-oxidation with either H_2O or CO_2 is never complete for such materials (as opposed to the re-oxidation with O_2). Accordingly, the presence of residual oxygen in the system when switching the gas atmosphere must be avoided in order to prevent the swift material re-oxidation. The observed mass gain may thus not be attributed to the CO_2 splitting, and quantifying the amount of produced CO by gas analysis would be necessary to confirm the results.

The $La_{1-x}Sr_xMn_{1-y}Fe_yO_3$ perovskite was also investigated [61]. The starting reduction temperature of this perovskite was reduced when increasing the Fe content, which in turn promoted the reduction extent. As an illustration, $La_{0.6}Sr_{0.4}Mn_{0.8}Fe_{0.2}O_3$ produced 286 µmol/g of O_2 at 1350 °C while $La_{0.6}Sr_{0.4}Mn_{0.2}Fe_{0.8}O_3$ produced 333 µmol/g. The CO amount produced tended to decrease with the increase of the Fe content. For instance, $La_{0.6}Sr_{0.4}MnO_3$ doped with 20% Fe produced 329 µmol/g of CO while $La_{0.6}Sr_{0.4}MnO_3$ doped with 60% Fe produced 277 µmol/g [61].

In order to improve the fuel production during the re-oxidation step, Mn substitution by Cr ion was investigated. $La_{0.7}Sr_{0.3}Mn_{0.7}Cr_{0.3}O_3$ was reported by Sugiyama et al. [57] to yield a similar O_2 production as $La_{0.7}Sr_{0.3}Mn_{0.7}Al_{0.3}O_3$ but a higher H_2 production. The presence of Cr in the B-site permits to increase the oxidation extent when compared to Al.

3.2. Lanthanum–Cobalt Perovskites

Lanthanum–cobalt perovskites were studied in thermochemical cycles. $LaCoO_3$ presents a high O_2 production (369 µmol/g at T_{red} = 1300 °C) during the first reduction step. However, the CO

production is low and it decreases quickly over cycles: 86 and 22 µmol/g of CO during the first and second cycles, respectively [38].

Lanthanum–cobalt perovskites substituted in the A or/and B-site were investigated. Regarding the impact of Ca dopant in the A-site, the increase of Ca content promoted oxygen production (715 µmol/g for $La_{0.8}Ca_{0.2}CoO_3$ and 1213 µmol/g for $La_{0.2}Ca_{0.8}CoO_3$ at 1300 °C). Figure 7a reveals that the increase of Ca content increases the O_2 production rate. Nonetheless, the hydrogen production dropped for Ca content above 40%, as shown in Figure 7b. For example, the hydrogen production was 587 µmol/g for 40% Ca content versus only 204 µmol/g for 80% Ca content at 900 °C. Wang et al. [62] selected $La_{0.6}Ca_{0.4}CoO_3$ as the most promising material among Ca-doped lanthanum–cobalt perovskites according to both O_2 and CO production.

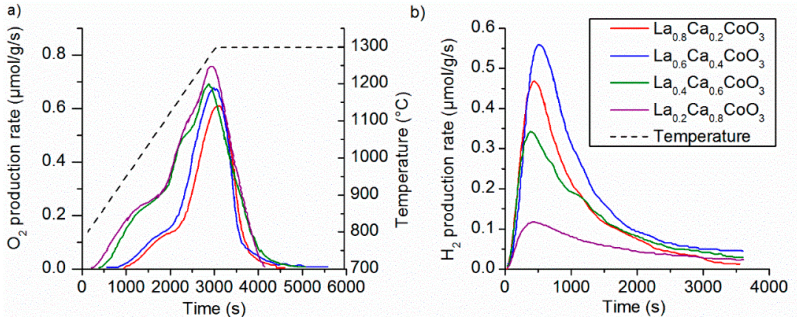

Figure 7. (**a**) O_2 production rate (T_{red} = 1350 °C) and (**b**) H_2 production rate (T_{ox} = 900 °C), for $La_{0.8}Ca_{0.2}CoO_3$, $La_{0.6}Ca_{0.4}CoO_3$, $La_{0.4}Ca_{0.6}CoO_3$, and $La_{0.2}Ca_{0.8}CoO_3$ [62].

Substitution of lanthanum by Sr in lanthanum–cobalt perovskites was also considered. The $La_{0.8}Sr_{0.2}CoO_3$ perovskite presents a mass loss (1.5%) higher than $La_{0.8}Sr_{0.2}MnO_3$ (0.1%), meaning a higher reduction extent [63]. Furthermore, $La_{0.6}Sr_{0.4}CoO_3$ offers higher H_2 production (514 µmol/g) than $La_{0.6}Sr_{0.4}MnO_3$ (234 µmol/g) [64]. However, Orfila et al. [63] tested the stability of this perovskite, highlighting a decrease of the production after four consecutive cycles. This is due to the formation of a pure Co oxide phase that impairs both O_2 and CO/H_2 production [63]. In addition, Demont et al. [32] pointed out a partial decomposition of the $La_{0.8}Sr_{0.2}CoO_3$ perovskite to form a Ruddlesden–Popper phase according to reaction (14). However, Ruddlesden–Popper phases are subjected to topotactic oxygen release which can be suitable for thermochemical cycles [32].

$$2(La,Sr)CoO_3 \rightarrow (La,Sr)_2CoO_4 + CoO + 1/2\ O_2 \quad (14)$$

Iron was also investigated as another dopant in lanthanum–cobalt perovskites. It appears that the presence of Fe decreases the oxygen production. For example, $LaCoO_3$ releases 369 µmol/g of O_2 at 1300 °C, whereas $LaFe_{0.75}Co_{0.25}O_3$ releases 59 µmol/g. In addition, the oxidation step was not enhanced by the introduction of Fe. Nair and Abanades [38] emphasized that the use of Fe as dopant in $LaCoO_3$ neither improves the perovskite stability, nor the re-oxidation yield. In addition to the use of Fe dopant in B-site, the introduction of Sr in the A-site was tested. The mix Co/Fe tends to increase the reduction extent (465 µmol/g O_2 for $La_{0.6}Sr_{0.4}Co_{0.2}Fe_{0.8}O_3$ at 1200 °C) compared to perovskite with the B-site only occupied by Fe (337 µmol/g O_2 for $La_{0.6}Sr_{0.4}FeO_3$ at 1200 °C). However, the produced amount of CO is low (90 µmol/g during the 1st cycle) and decreases over cycles (51 µmol/g during the 2nd cycle) due to sintering [32,38].

$La_{1-x}Sr_xCo_{1-y}Cr_yO_3$ was also studied for fuel production. Above 50% of Co, the powder grain size increased. Bork et al. [65] noticed that the increase of Co content promoted the O_2 production. In addition, increasing the Co content up to 20% increased the CO production. An optimum composition was thus deduced for fuel production: $La_{0.6}Sr_{0.4}Co_{0.2}Cr_{0.8}O_3$. This perovskite offered a CO production of 157 µmol/g with a reduction temperature of 1200 °C and an oxidation temperature of 800 °C. This performance is similar to ceria (CO production: 168 µmol/g) with

reduction and oxidation temperatures of 1500 °C and 1000 °C, respectively. Thus, comparable CO production as ceria can be obtained with $La_{0.6}Sr_{0.4}Co_{0.2}Cr_{0.8}O_3$ at lower temperatures. In addition, Bork et al. [65] demonstrated the absence of carbonate formation during the oxidation step in presence of CO_2, confirming the ability of $La_{0.6}Sr_{0.4}Co_{0.2}Cr_{0.8}O_3$ to be used in thermochemical cycles.

3.3. Yttrium–Manganese Perovskites

Strontium was studied as a B-site dopant in yttrium manganese perovskites. $Y_{0.5}Sr_{0.5}MnO_3$ shows a reduction extent higher (539 µmol/g of O_2 produced) than $La_{0.5}Sr_{0.5}MnO_3$, (256 µmol/g of O_2 produced) in similar conditions [49]. The improvement of the reduction extent can be explained by a smaller ionic radius of Y^{3+} ($r = 1.08$ *A* [40]) than La^{3+} ($r = 1.36$ *A* [40]). This smaller ionic radius has for effect an increase of the MnO_6 octahedron inclination and an increase of the lattice distortion, which promotes oxygen departure [46]. Demont and Abanades [41] observed that the O_2 production peak was reached at 1315 °C (Figure 5a), suggesting that the reduction temperature can be lowered without diminishing the O_2 production. Dey et al. [46] reported a complete re-oxidation, performed with thermogravimetric analysis. Nevertheless, the extremely fast oxidation profile can again be questioning, suggesting possible prompt reaction with residual O_2 instead of CO_2. Rodenbough and Chan [66] performed a thermochemical cycle in similar conditions as the one used by Dey et al. [46] and they analyzed the output gas with integrated IR-electrochemical sensor to detect CO. They observed a lack of CO and they suggested that the mass uptake observed by Dey et al. [46] was not attributable to the CO_2 splitting [66]. Nair and Abanades [49] also pointed out a low re-oxidation yield (14%), which is in agreement with Rodenbough and Chan [66].

Substitution of yttrium by calcium was also investigated, yielding $Y_{1-x}Ca_xMnO_3$ perovskite. Both yttrium and calcium tend to increase the reduction extent in comparison with lanthanum and strontium, respectively. The O_2 production was 573 µmol/g for $Y_{0.5}Ca_{0.5}MnO_3$ (at T_{red} = 1400 °C) while it was only 312 µmol/g and 481 µmol/g for $La_{0.5}Ca_{0.5}MnO_3$ and $Y_{0.5}Sr_{0.5}MnO_3$, respectively [46].

3.4. Other Perovskites

The most largely investigated perovskite series were presented in the previous sections. Other perovskites were also investigated as reactive materials in thermochemical cycles such as $BaMn_{1-y}Ce_yO_3$. It was highlighted that the $BaCe_{0.25}Mn_{0.75}O_3$ formulation haD higher reduction ability than ceria for a temperature below 1400 °C. Furthermore, this perovskite produces three times more hydrogen (140 µmol/g) than ceria with a reduction temperature of 1350 °C and an oxidation temperature of 850 °C. Compared with $La_{0.6}Sr_{0.4}Mn_{0.6}Al_{0.4}O_3$ perovskite, $BaCe_{0.25}Mn_{0.75}O_3$ offers similar production, but its oxidation kinetics are faster. Barcellos et al. [67] investigated the ability of this material to produce hydrogen under high-conversion conditions. The H_2O:H_2 ratio required to drive the thermochemical cycle has to be below 1000:1. To realize this condition, different H_2O:H_2 ratios were used in the reaction chamber. $La_{0.6}Sr_{0.4}Mn_{0.6}Al_{0.4}O_3$ showed a rapid decrease of H_2 production with the decrease of H_2O:H_2 ratio and hydrogen production stopped for H_2O:$H_2 < 500$, whereas $BaCe_{0.25}Mn_{0.75}O_3$ also showed a decrease of H_2 production as the H_2O:H_2 ratio decreased but it still had comparable H_2 production as ceria with a H_2O:H_2 ratio of 285. The fuel productions for $La_{0.6}Sr_{0.4}Mn_{0.6}Al_{0.4}O_3$, $BaCe_{0.25}Mn_{0.75}O_3$, and ceria under various H_2O:H_2 ratios are illustrated in Figure 8. Thus, $BaCe_{0.25}Mn_{0.75}O_3$ perovskite is able to perform water splitting under milder conditions in the aim of future large-scale implementation [67].

The influence of the cation in A-site was studied by Dey et al. [46] who tested a set of perovskites in the series $Ln_{0.5}A_{0.5}MnO_3$ (Ln = La, Nd, Sm, Gd, Dy, Y, and A = Sr, Ca). They showed that the decrease of the rare-earth ionic size improves the reduction extent. Consequently, the maximal O_2 production was reached by $Y_{0.5}Ca_{0.5}MnO_3$ (573 µmol/g) and $Y_{0.5}Sr_{0.5}MnO_3$ (481 µmol/g), because yttrium has the smallest ionic radius among the rare-earth tested. As a comparison, $La_{0.5}Ca_{0.5}MnO_3$ and $La_{0.5}Sr_{0.5}MnO_3$ produced 312 µmol/g and 198 µmol/g of O_2, respectively, in the same experimental conditions (T_{red} = 1400 °C). The decrease of the rare-earth ionic size leads to a decrease in the tolerance

factor. This increases the tilting of the MnO_6 octahedron in the perovskite structure and the lattice distortion, and this favors the oxygen departure. However, the re-oxidation step of perovskites was found to be very fast and almost complete (over 500 µmol/g of produced CO for an oxidation temperature of 1100 °C). On the contrary, Nair and Abanades [38] found that the re-oxidation yield was very low (10% for $Y_{0.5}Sr_{0.5}MnO_3$). The very low re-oxidation extent for $Y_{0.5}Sr_{0.5}MnO_3$ in comparison with $La_{0.5}Sr_{0.5}MnO_3$ and $La_{0.5}Ca_{0.5}MnO_3$ can be observed in Figure 9.

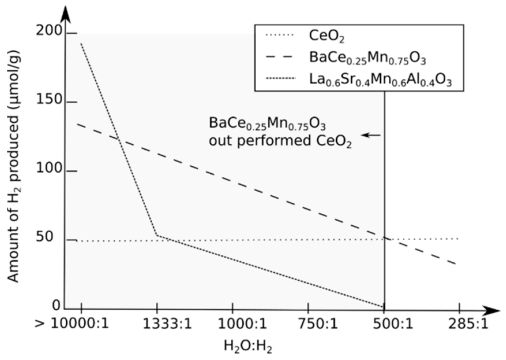

Figure 8. H_2 production as function of the H_2O:H_2 ratio for $La_{0.6}Sr_{0.4}Mn_{0.6}Al_{0.4}O_3$, $BaCe_{0.25}Mn_{0.75}O_3$, and ceria at T_{red} = 1350 °C and T_{ox} = 850 °C (adapted from Reference [67]).

The $Ba_{1-x}Sr_xFeO_3$ perovskite was also studied for thermochemical cycles. This perovskite showed a high reduction extent (582 µmol/g of O_2 produced) with a low reduction temperature (1000 °C), and it was able to produce CO (136 µmol/g) in an isothermal cycle (1000 °C). Nevertheless, a low stability was observed for this perovskite, with decreasing CO production [38].

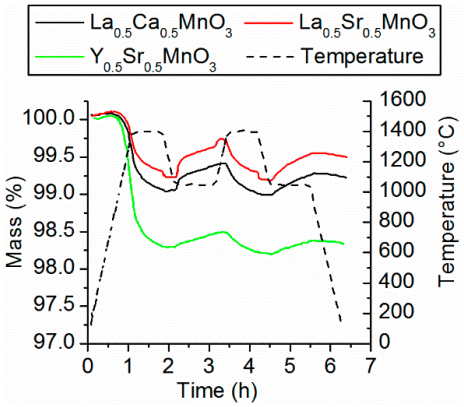

Figure 9. TGA of $La_{0.5}Sr_{0.5}MnO_3$, $La_{0.5}Ca_{0.5}MnO_3$, and $Y_{0.5}Sr_{0.5}MnO_3$ during two thermochemical cycles (T_{red} = 1400 °C and T_{ox} = 1050 °C) [38].

Wang et al. [64] studied the impact of the cation (Cr, Mn, Fe, Ni, and Co) occupying the B-site of Sr-doped lanthanum perovskites. They reported that the $La_{0.6}Sr_{0.4}CoO_3$ perovskite can accommodate more oxygen vacancies than $La_{0.6}Sr_{0.4}BO_3$ perovskites (with B = Cr, Mn, Fe, and Ni), which is due to a low energy of oxygen vacancy formation. Furthermore, $La_{0.6}Sr_{0.4}CoO_3$ presents a lower onset temperature (~900 °C) than $La_{0.6}Sr_{0.4}MnO_3$ (~1020 °C) in similar conditions. The reported hydrogen production is also higher for $La_{0.6}Sr_{0.4}CoO_3$ (514 µmol/g) at 900 °C (with T_{red} = 1300 °C) than for other $La_{0.6}Sr_{0.4}BO_3$ perovskites (Ni: 368 µmol/g; Fe: 349 µmol/g; Cr: 280 µmol/g and Mn: 234 µmol/g) [64].

To date, a large number of perovskite formulations have been studied for thermochemical cycles, and some important results are summarized in Table 1. Perovskites can accommodate to a wide range of oxygen non-stoichiometry. However, the high vacancy formation ability is usually associated to a slow re-oxidation step, impeding complete re-oxidation and resulting in low CO/H_2 production rates.

In other words, a favored reduction capability can be obtained at the expense of lower oxidation extent and vice-versa. A compromise between maximum achievable oxygen non-stoichiometry and fuel production yield has to be considered, and the key outcomes may arise from an optimization of the perovskite's composition. The recent results presented above show that the high number of possible perovskite formulations leaves space for the finding of suitable materials for thermochemical cycles.

Table 1. Comparison of the performance of current perovskites studied for thermochemical cycles.

Material	Synthesis Method	Experimental Conditions	Production (μmol/g)		Ref.
			O_2	H_2/CO	
$La_{0.7}Sr_{0.3}Mn_{0.7}Cr_{0.3}O_3$	Modified Pechini	Reduction: 1350 °C under N_2 Oxidation: H_2O between 50 and 84%; 1000 °C during 60 min	~98	~107	[57]
$LaFe_{0.75}Co_{0.25}O_3$	Solid-state	Reduction: 1300 °C under Ar Oxidation: 50% CO_2 in Ar at 1000 °C	59	117	[38]
$LaCoO_3$	Solid-state	Reduction: 1300 °C under Ar Oxidation: 50% CO_2 in Ar at 1000 °C	369	123	[38]
$Ba_{0.5}Sr_{0.5}FeO_3$	Solid-state	Reduction: 1000 °C under Ar Oxidation: 50% CO_2 in Ar at 1000 °C	582	136	[38]
$La_{0.6}Sr_{0.4}Co_{0.2}Cr_{0.8}O_3$	Pechini	Reduction: 1200 °C under Ar Oxidation: 50% CO_2 in Ar at 800 °C	-	157	[65]
$La_{0.4}Ca_{0.6}Mn_{0.6}Al_{0.4}O_3$	Modified Pechini	Reduction: 1400 °C under Ar Oxidation: 40% H_2O in Ar at 1000 °C	231	429	[58]
$BaCe_{0.25}Mn_{0.75}O_3$	Modified Pechini	Reduction: 1350 °C under Ar Oxidation: 40% H_2O in Ar at 1000 °C	-	135	[67]
$La_{0.5}Sr_{0.5}MnO_3$	Solid-state	Reduction: 1400 °C under Ar Oxidation: H_2O at 1000 °C	298	195	[32]
$La_{0.35}Sr_{0.75}MnO_3$	Commercial powder	Reduction: 1400 °C under Ar Oxidation: H_2O at 1050 °C	166	124	[32]
$La_{0.5}Ca_{0.5}MnO_3$	Solid-state	Reduction: 1400 °C under Ar Oxidation: 50% CO_2 at 1050 °C	311	210	[41]
$La_{0.5}Ba_{0.5}MnO_3$	Solid-state	Reduction: 1400 °C under Ar Oxidation: 50% CO_2 at 1050 °C	203	185	[41]
$La_{0.5}Sr_{0.5}Mn_{0.4}Al_{0.6}O_3$	Pechini	Reduction: 1400 °C under Ar Oxidation: 50% CO_2 at 1050 °C	246	279	[41]
$La_{0.5}Sr_{0.5}Mn_{0.83}Mg_{0.17}O_3$	Solid-state	Reduction: 1400 °C under Ar Oxidation: 50% CO_2 at 1050 °C	214	209	[41]
$La_{0.5}Sr_{0.5}MnO_3$	Pechini	Reduction: 1400 °C under Ar Oxidation: 50% CO_2 at 1050 °C	256	256	[49]
$Y_{0.5}Sr_{0.5}MnO_3$	Pechini	Reduction: 1400 °C under Ar Oxidation: 50% CO_2 at 1050 °C	539	101	[49]
$La_{0.6}Sr_{0.4}Mn_{0.6}Al_{0.4}O_3$	Modified Pechini	Reduction: 1400 °C under Ar Oxidation: 40% CO_2 at 1000 °C	-	307	[51]
$La_{0.6}Ca_{0.4}Mn_{0.6}Al_{0.4}O_3$	Modified Pechini	Reduction: 1240 °C under Ar Oxidation: 50% CO_2 at 850 °C	165	230	[50]
$La_{0.6}Sr_{0.4}Mn_{0.6}Al_{0.4}O_3$	Modified Pechini	Reduction: 1240 °C under Ar Oxidation: 50% CO_2 at 850 °C	190	245	[50]
$La_{0.6}Ca_{0.4}Mn_{0.8}Ga_{0.2}O_3$	Modified Pechini	Reduction: 1300 °C Oxidation: H_2O at 900 °C	212	401	[59]
$La_{0.5}Sr_{0.5}Mn_{0.95}Sc_{0.05}O_3$	-	Reduction: 1400 °C under Ar Oxidation: 40% CO_2 at 1100 °C	417	545	[60]
$La_{0.6}Sr_{0.4}Mn_{0.8}Fe_{0.2}O_3$	Modified Pechini	Reduction: 1350 °C under N_2 Oxidation: CO_2 at 1000 °C	286	329	[61]
$La_{0.6}Sr_{0.4}CoO_3$	Modified Pechini	Reduction: 1300 °C Oxidation: 40% H_2O at 900 °C	718	514	[64]
$La_{0.6}Ca_{0.4}CoO_3$	Modified Pechini	Reduction: 1300 °C Oxidation: 40% H_2O at 900 °C	715	587	[62]
$Y_{0.5}Ca_{0.5}MnO_3$	Solid state	Reduction: 1400 °C Oxidation: CO_2 at 1100 °C	573	671	[46]

4. Kinetic Studies

Thermodynamic limitations define the theoretical bounds of fuel production, whereas kinetic limitations determine the maximum fuel amount that can be produced in a reasonable duration. Different methods were used to investigate the kinetics of redox reactions involving perovskites. Here, an overview of the methods used is proposed with their advantages and drawbacks.

The kinetic rate of a solid–gas reaction can be expressed with the relation (15),

$$\frac{\mathrm{d}\alpha}{\mathrm{dt}} = A \exp\left(-\frac{E_a}{RT}\right) f(\alpha) \tag{15}$$

where α is the conversion ratio, A the pre-exponential factor, E_a the activation energy, R the gas constant, T the reaction temperature, and f the function representing the reaction model. The activation energy represents the energy barrier that needs to be overcome to initiate the reaction, whereas $f(\alpha)$ is a mathematical representation of the reaction mechanism [68]. Physical reaction processes can be expressed in a mathematical function $f(\alpha)$, supplementary detailed information are available elsewhere [69]. A complete kinetic study is generally required to determine the triplet of the following parameters: E_a, A, and f.

In their study, Demont and Abanades [17,20] determined the activation energy during the reduction step with linear fits using Arrhenius expression. To determine the conversion fraction, they used the mass variation between the initial state and the mass at the time t over the mass variation between initial and final states. The Equation (16) can be used to determine the kinetic parameters.

$$\ln\left(\frac{d\alpha}{dt}\frac{1}{f(\alpha)}\right) = -\frac{E_a}{RT} + \ln A \tag{16}$$

A contracting sphere model was used for the reaction model, i.e., $f(\alpha) = 3(1-\alpha)^{\frac{2}{3}}$, which was previously validated by Reference [26]. Thanks to this method, an activation energy of 158, 145, and 174 kJ/mol was obtained for $La_{0.5}Ca_{0.5}MnO_3$, $La_{0.5}Sr_{0.5}MnO_3$, and $La_{0.5}Ba_{0.5}MnO_3$ reduction, respectively [41]. Jiang et al. [70] also used this method to determine the activation energy. However, they tested four different reaction models and all the models fit properly to the experimental data, which prevents determining kinetic model. Because each model results in a different activation energy, the authors determined an activation energy range [70]. This simple method allows obtaining the activation energy easily and quickly. Conversely, only a part of the reaction in a given temperature range was taken into account to calculate the activation energy. Furthermore, this method is relevant only if there is one step in the reaction mechanism and it requires knowing the reaction model. Thus, it is suitable to obtain a first estimation of the activation energy.

In order to study the kinetics of the oxidation step in isothermal conditions, Jiang et al. [70] used a master plot method. The conversion rate data in differential form is normalized using a reference point at α = 0.5, as represented by the Equation (17).

$$\frac{(\mathrm{d}\alpha/\mathrm{d}t)}{(\mathrm{d}\alpha/\mathrm{d}t)_{\alpha=0.5}} = \frac{f(\alpha)}{f(\alpha)_{\alpha=0.5}} \tag{17}$$

A comparison between the normalized experimental data and different theoretical functions of solid-state reaction models, enables to identify the appropriate reaction model, as illustrated in Figure 10. Using this method, Jiang et al. [70] found that the best fitting model at 1000 °C is the first order diffusion model (D1), whereas the first order reaction (F1) is the best model at 1100 °C, for CO production by $LaFe_{0.7}Co_{0.3}O_3$ [70]. The master plot method is suited to identify the reaction model with only one experimental test in isothermal condition. However, supplementary kinetic analyses are required to identify the other kinetic parameters [71,72].

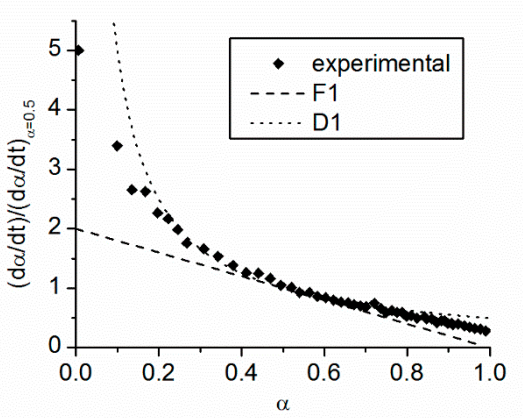

Figure 10. Experimental data compared to first order reaction model (F1) and first order diffusion model (D1) for CO production at 1000 °C by $LaFe_{0.7}Co_{0.3}O_3$ [70].

McDaniel et al. [73] used another approach to study perovskite oxidation kinetics, which was first developed by Scheffe et al. [74] to study cobalt ferrite. It consists in separating the oxidation kinetic rate in different contributions:

1. Kinetic rate related to the oxidation reaction itself;
2. Time necessary for the oxidant gas to be introduced in the reaction chamber;
3. Gas detector delay;
4. Influence of the dispersion of the gas product during the transportation between the reactor outlet and the detector.

The introduction of the oxidant is modeled as a step function (Figure 11a). The step function shape is determined using a numerical simulation of the reactor inlet for different operating conditions. The solid-state reaction is described by a theoretical kinetic model in Equation (18).

$$\frac{d\alpha}{dt} = A \exp\left(-\frac{E_a}{RT}\right) \left[Y_{H_2O}(t)\right]^{\gamma} f(\alpha) \quad (18)$$

where Y_{H_2O} is the mole fraction of the oxidant gas in the inlet and γ is the factor that rules the relation with the gaseous oxidant concentration. The H_2 production rate is determined thanks to a solid state model as a function of time (Figure 11b). Afterward, this signal is introduced into a series of ideal continuously-stirred tank reactors (CSTR) to simulate the dispersion and mixing of gas product ((Figure 11c). Kinetic model and associated parameters are obtained thanks to the least-squares method. The experimental H_2 production rates are fitted to the simulation using different kinetic models, with the least-squares method to obtain the kinetic model and the associated activation energy. If a single kinetic model does not fit correctly with the experimental data, two kinetic models acting in parallel are used [73]. Details about the model have been provided elsewhere [74]. For instance, Arifin and Weimer [75] managed to identify the following parameters for the water splitting with ceria thanks to this method: $A = 1\ s^{-1}$; $E_a = 29$ kJ/mol; $\gamma = 0.89$ and $f(\alpha) = (1 - \alpha)$. However, they did not manage to compute properly these parameters for carbon dioxide splitting with the same material [75]. This method permits to calculate all the kinetic parameters at the same time, by taking into account the influence of physical processes which depend on the experimental setup. However, numerical simulation of the reactor and calculations to fit the experimental data are required, then providing an appropriate method to precisely study the oxidation kinetics.

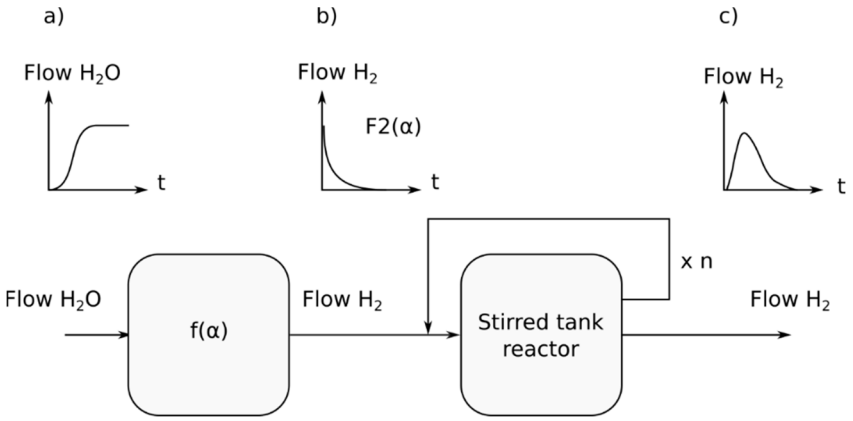

Figure 11. Schematic representation of the kinetic model used by McDaniel et al. [73], (**a**) step function of the oxidant flow introduction, (**b**) H_2 evolution profile from solid state model, (**c**) H_2 flow rate after mixing and dispersion in a continuously-stirred tank reactor.

Kim et al. [76] studied the surface reaction kinetics and measured the electrical conductivity relaxation of a thin film of $La_{1-x}Sr_xMnO_3$. Two electrodes (Pt) were placed on the $La_{1-x}Sr_xMnO_3$ (x = 0.1, 0.2, 0.3 and 0.4) coating. The sample was placed in a furnace tube swept by a CO/CO_2 mixture. The sample was first heated until thermal equilibrium, and then the oxygen partial pressure was suddenly changed. The oxygen content is related to the plane conductivity in the thin film, which was measured until reaching the new equilibrium of the sample. Measurements were performed for both reduction and oxidation in order to support the hypothesis of first order surface oxygen exchange reaction and the conductivity varied linearly with the oxygen partial pressure. Experimental data were fitted with Equation (19),

$$\frac{\sigma(t) - \sigma(0)}{\sigma(\infty) - \sigma(0)} = 1 - \exp\left(\frac{k_s}{a}t\right) \tag{19}$$

where σ represents the conductivity as a function of time, k_s is the solid-state constant rate and a is the film thickness. From both Equation (19) and experimental data, the solid-state reaction rate constant k_s can be extracted. This method permits to study only surface oxygen exchange and not oxygen diffusion in the bulk, as the coating thickness is much thinner than the critical thickness for bulk diffusion. Thanks to this method, Kim et al. [76] computed the k_s values for a set of $La_{1-x}Sr_xMnO_3$ perovskites with different dopant contents, in order to investigate the effect of Sr concentration, temperature, and oxygen partial pressure on the surface kinetics [76]. This method yields the values of k_s constant with good accuracy. Nonetheless, it is necessary to prepare coated samples for this method and a device able to measure the electrical conductivity relaxation.

Yang et al. [30] investigated the limiting rate mechanism in the oxidation reaction for different dopant levels in perovskites. They studied the different parameters that can limit the oxidation kinetic including the morphology, the oxygen diffusion rate and the surface reactions. They performed thermochemical cycles in a furnace and analyzed the output gas for a series of perovskites. Concerning the influence of morphology, a comparison was performed between the grain size and the peak production rate evolution. If the grain size decreases, the production rate should increase due to enhanced available surface area for the reaction. Otherwise, the morphology would not limit the oxidation kinetic. Afterward, the authors investigated whether the oxygen diffusion is the limiting step. They checked whether an increase of the oxygen diffusivity due to Sr content change corresponds to an increase of the oxidation rate. The diffusivity is defined as Equation (20),

$$D_{chem} = D_{V_o} t_{el} \left(-\frac{1}{2} \frac{\partial \ln p^*_{O_2}}{\partial \ln [V_O^{\cdot\cdot}]} \right) = D_{V_o} t_{el} \Lambda \tag{20}$$

where D_{chem} is the chemical diffusivity; D_{V_O} is the vacancy diffusivity, t_{el} is the transference number of electronic species and $\left[V_O^{\cdot\cdot}\right]$ is the fractional oxygen vacancy (with Kröger–Vink notation). D_{V_o} and t_{el} are independent from the oxygen partial pressure and the composition. D_{chem} is then directly related to Λ defined by the Equation (21).

$$\Lambda = -\frac{1}{2}\frac{\partial \ln p^*_{O_2}}{\partial \ln\left[V_O^{\cdot\cdot}\right]} \tag{21}$$

The Λ values can be computed as a function of the oxygen partial pressure for the different perovskites. In case diffusion is the limiting step, Λ should increase with the increase of the production rate. Otherwise, it can be assumed that it is not the limiting step. To characterize the surface reaction step, the authors used the oxygen flux through the surface, J_o, defined as follows:

$$J_O = -k_{surf}\Delta C_o \tag{22}$$

where J_o is the oxygen flow through the surface, k_{surf} is the surface reaction rate constant, ΔC_o is the difference between the oxygen surface concentration and the gas oxygen concentration, directly proportional to $\Delta\delta$. The reaction is assumed to be of first order and k_{surf} independent from the concentration. In Equation (22), the driving force is the difference in concentration. In thermodynamics, driving forces are represented by the difference in oxygen chemical potential, $\Delta\mu_o$, defined by Equation (23).

$$\Delta\mu_o = \mu_{O,solid}(interface) - \mu_{o,gas}(interface) \tag{23}$$

ΔC_o is directly proportional to $\Delta\delta$, while $\mu_o = \mu_o^0 + RT\ln p_{O_2}$, $\Delta\mu_o$ is the difference in effective oxygen partial pressure between the quenched state and the oxidized state at the same temperature. Afterward, the plot of the oxidation production peak as function of the non-stoichiometry and the plot of the oxidation production peak as a function of $\Delta\mu_O$ for each perovskite, permit to determine if the surface reaction step is the limiting step. If the oxidation peak production rate increases with the $\Delta\mu_O$ increase and the $\Delta\delta$ decrease, the oxidation is then limited by the surface reaction step. With this method, Yang et al. [30] revealed that the oxidation step for $La_{1-x}Sr_xMnO_3$ is limited by the solid-state reaction. The interest of this method is to determine the limiting step during the oxidation reaction and to highlight the effect of the dopant on kinetics. It only requires few materials with different dopant levels. Regarding main drawback, the constants like k_{surf} or k_s cannot be computed.

Davenport et al. [24,77,78] developed a thermo-kinetic model. Assuming that O_2 production takes place under quasi-equilibrium conditions, the O_2 production is entirely governed by the thermodynamic properties. Applying mass balance to the oxygen release and taking in equilibrium, they expressed the oxygen flow rate as:

$$\dot{v}_{O_2}(t) = \frac{\dot{V}_{red}}{m_{CeO_2}}\frac{\left(P_{O_2}(\delta,T) - P_{O_2,in}\right)}{\left(P_{tot} - P_{O_2}(\delta,T)\right)} \tag{24}$$

where V_{red} is the volumetric flow rate of reducing gas, m_{CeO_2} is ceria mass used, P_{tot} is the total pressure, $P_{O_2,in}$ is the oxygen partial pressure at the inlet, and $P_{O_2}(\delta,T)$ is the oxygen partial pressure in equilibrium at a non-stoichiometry of δ. Concerning the oxidation rate, a similar expression is obtained by applying the mass balance constraints on water, hydrogen and oxygen:

$$\dot{v}_{H_2} = -\frac{\dot{V}_{ox}}{m_{CeO_2}}\frac{\left(2P_{O_2}(\delta,T)\hat{P}_{O_2}(\delta,T)^{\frac{1}{2}} + 2P_{O_2}(\delta,T)K_{H_2O} - \chi_{H_2O}K_{H_2O,T}\left(P_{tot} - P_{O_2}(\delta,T)\right)\right)}{\left(\hat{P}_{O_2}(\delta,T)^{\frac{1}{2}} + K_{H_2O,T}\right)\left(P_{tot} - P_{O_2}(\delta,T)\right)} \tag{25}$$

where $\dot{v}_{H_2}$ is the normalized flow rate of hydrogen, $\dot{V}_{ox}$ corresponds to the volumetric flow rate of oxidant gas; χ_{H_2O} is the molar ratio of H_2O in the oxidizing gas; $\hat{P}$ is P/P_{ref} and $K_{H_2O,T}$ is the equilibrium constant for water thermolysis. Details about the method for obtaining the Equations (24)

and (25) can be found elsewhere [77]. In Equations (24) and (25), the only unknown remaining is $P_{O_2}(\delta, T)$ which can be computed thanks to Equation (26).

$$\frac{1}{2}\ln\left(P_{O_2}(\delta, T)\right) = \frac{-\Delta H_{red}(\delta) + T\Delta S_{red}(\delta)}{RT} \quad (26)$$

The thermodynamic properties used in Equation (26) can be found in the literature. By this way, the gas flow rates of O_2 and H_2 can be computed by iteration. Using this method, Davenport et al. [24] showed that the oxidation rate of porous ceria is limited by the gas flow introduced in the reactor when the oxidant gas flow is under 600 $Ncm^3/min/g$ and the oxidation temperature above 1200 °C. This model shows good agreement with the experimental data when at high temperatures and moderate gas flow rates. However, the kinetic study of a reaction with this model requires that the reaction occurs under quasi-equilibrium condition, to assume that the reaction rate is ruled by the thermo-kinetic model.

5. Conclusions

Thermochemical redox cycles are promising for converting solar energy into chemical energy in the form of sustainable solar fuels that can be stored long-term, transported long-range, and used on-demand. In order to enhance global energy conversion efficiency, the optimization of the reactive material is required. Perovskites represent a promising class of materials for thermochemical fuel production cycles. Such materials have a high thermal stability and can accommodate large oxygen non-stoichiometry in their structure owing to high oxygen exchange properties, thereby allowing for large fuel production. Furthermore, the reduction temperature can be decreased compared with other materials like ceria, while keeping comparable fuel productivities. The main drawback associated with the use of perovskites is generally the incomplete re-oxidation yield due to low kinetics and low thermodynamic driving forces. The large number of possible perovskite formulations and the discovery of novel materials make possible tuning the redox properties to optimize the fuel production. Perovskites based on lanthanum–manganese, lanthanum–cobalt, yttrium–manganese associated with different dopants (Al, Ga, Ba, Mg, Sr, Ca, Ce, Cr, Fe) are the principal materials that were studied for thermochemical cycles application. Moreover, different methods used to study reaction kinetics involving non-stoichiometric perovskites were reported here to provide insights into the different available techniques with their advantages and drawbacks and the related performance data. In showing that perovskites constitute a promising class of materials in the context of solar thermochemical fuel production, further advancements in the discovery and characterization of new and better performing redox materials are of critical importance, while complying with the necessary attributes related to favorable thermodynamics, rapid reaction kinetics, and crystallographic stability over thermochemical cycling.

Author Contributions: Writing—Original Draft Preparation, A.H.; Writing—Review & Editing, S.A., A.J., J.J.; Supervision, S.A., A.J.; Project Administration, S.A.; Funding Acquisition, S.A.

Acknowledgments: This study was supported by the French National Agency for Research (ANR, SUNFUEL project, contract N° ANR-16-CE06-0010).

Conflicts of Interest: The authors declare no conflict of interest.

References

1. Ashby, M.F. Chapter 12—Materials for low-carbon power. In *Materials and the Environment (Second Edition)*; Ashby, M.F., Ed.; Butterworth-Heinemann: Boston, MA, USA, 2013; pp. 349–413. ISBN 978-0-12-385971-6.
2. Marxer, D.; Furler, P.; Scheffe, J.; Geerlings, H.; Falter, C.; Batteiger, V.; Sizmann, A.; Steinfeld, A. Demonstration of the Entire Production Chain to Renewable Kerosene via Solar Thermochemical Splitting of H_2O and CO_2. *Energy Fuels* **2015**, *29*, 3241–3250. [CrossRef]

3. Marxer, D.; Furler, P.; Takacs, M.; Steinfeld, A. Solar thermochemical splitting of CO_2 into separate streams of CO and O_2 with high selectivity, stability, conversion, and efficiency. *Energy Environ. Sci.* **2017**, *10*, 1142–1149. [CrossRef]
4. Siegel, N.P.; Miller, J.E.; Ermanoski, I.; Diver, R.B.; Stechel, E.B. Factors Affecting the Efficiency of Solar Driven Metal Oxide Thermochemical Cycles. *Ind. Eng. Chem. Res.* **2013**, *52*, 3276–3286. [CrossRef]
5. Muhich, C.L.; Ehrhart, B.D.; Al-Shankiti, I.; Ward, B.J.; Musgrave, C.B.; Weimer, A.W. A review and perspective of efficient hydrogen generation via solar thermal water splitting. *Wiley Interdiscip. Rev. Energy Environ.* **2016**, *5*, 261–287. [CrossRef]
6. Carrillo, R.J.; Scheffe, J.R. Advances and trends in redox materials for solar thermochemical fuel production. *Solar Energy* **2017**, *156*, 3–20. [CrossRef]
7. Bhosale, R.R.; Takalkar, G.; Sutar, P.; Kumar, A.; AlMomani, F.; Khraisheh, M. A decade of ceria based solar thermochemical H_2O/CO_2 splitting cycle. *Int. J. Hydrogen Energy* **2018**. [CrossRef]
8. Chueh, W.C.; Haile, S.M. A thermochemical study of ceria: Exploiting an old material for new modes of energy conversion and CO_2 mitigation. *Philos. Trans. R. Soc. A Math. Phys. Eng. Sci.* **2010**, *368*, 3269–3294. [CrossRef] [PubMed]
9. Call, F.; Roeb, M.; Schmücker, M.; Sattler, C.; Pitz-Paal, R. Ceria Doped with Zirconium and Lanthanide Oxides to Enhance Solar Thermochemical Production of Fuels. *J. Phys. Chem. C* **2015**, *119*, 6929–6938. [CrossRef]
10. Le Gal, A.; Abanades, S. Dopant Incorporation in Ceria for Enhanced Water-Splitting Activity during Solar Thermochemical Hydrogen Generation. *J. Phys. Chem. C* **2012**, *116*, 13516–13523. [CrossRef]
11. Scheffe, J.R.; Jacot, R.; Patzke, G.R.; Steinfeld, A. Synthesis, Characterization, and Thermochemical Redox Performance of Hf^{4+}, Zr^{4+}, and Sc^{3+} Doped Ceria for Splitting CO_2. *J. Phys. Chem. C* **2013**, *117*, 24104–24114. [CrossRef]
12. Yadav, D.; Banerjee, R. A review of solar thermochemical processes. *Renew. Sustain. Energy Rev.* **2016**, *54*, 497–532. [CrossRef]
13. Romero, M.; Steinfeld, A. Concentrating solar thermal power and thermochemical fuels. *Energy Environ. Sci.* **2012**, *5*, 9234. [CrossRef]
14. Miller, J.E.; McDaniel, A.H.; Allendorf, M.D. Considerations in the Design of Materials for Solar-Driven Fuel Production Using Metal-Oxide Thermochemical Cycles. *Adv. Energy Mater.* **2014**, *4*, 1300469. [CrossRef]
15. Scheffe, J.R.; Steinfeld, A. Oxygen exchange materials for solar thermochemical splitting of H_2O and CO_2: A review. *Mater. Today* **2014**, *17*, 341–348. [CrossRef]
16. Kubicek, M.; Bork, A.H.; Rupp, J.L.M. Perovskite oxides—A review on a versatile material class for solar-to-fuel conversion processes. *J. Mater. Chem. A* **2017**, *5*, 11983–12000. [CrossRef]
17. Sunarso, J.; Hashim, S.S.; Zhu, N.; Zhou, W. Perovskite oxides applications in high temperature oxygen separation, solid oxide fuel cell and membrane reactor: A review. *Prog. Energy Combust. Sci.* **2017**, *61*, 57–77. [CrossRef]
18. Takacs, M.; Hoes, M.; Caduff, M.; Cooper, T.; Scheffe, J.R.; Steinfeld, A. Oxygen nonstoichiometry, defect equilibria, and thermodynamic characterization of $LaMnO_3$ perovskites with Ca/Sr A-site and Al B-site doping. *Acta Mater.* **2016**, *103*, 700–710. [CrossRef]
19. Meredig, B.; Wolverton, C. First-principles thermodynamic framework for the evaluation of thermochemical H_2O—Or CO_2—Splitting materials. *Phys. Rev. B* **2009**, *80*. [CrossRef]
20. Takacs, M.; Scheffe, J.R.; Steinfeld, A. Oxygen nonstoichiometry and thermodynamic characterization of Zr doped ceria in the 1573–1773 K temperature range. *Phys. Chem. Chem. Phys.* **2015**, *17*, 7813–7822. [CrossRef]
21. Al-Shankiti, I.; Ehrhart, B.D.; Weimer, A.W. Isothermal redox for H_2O and CO_2 splitting—A review and perspective. *Solar Energy* **2017**, *156*, 21–29. [CrossRef]
22. Bulfin, B.; Vieten, J.; Agrafiotis, C.; Roeb, M.; Sattler, C. Applications and limitations of two step metal oxide thermochemical redox cycles; a review. *J. Mater. Chem. A* **2017**, *5*, 18951–18966. [CrossRef]
23. Scheffe, J.R.; Weibel, D.; Steinfeld, A. Lanthanum–Strontium–Manganese perovskites as redox materials for solar thermochemical splitting of H_2O and CO_2. *Energy Fuels* **2013**, *27*, 4250–4257. [CrossRef]
24. Davenport, T.C.; Kemei, M.; Ignatowich, M.J.; Haile, S.M. Interplay of material thermodynamics and surface reaction rate on the kinetics of thermochemical hydrogen production. *Int. J. Hydrogen Energy* **2017**, *42*, 16932–16945. [CrossRef]

25. Evdou, A.; Zaspalis, V.; Nalbandian, L. $La_{(1-x)}Sr_xMnO_{3-\delta}$ perovskites as redox materials for the production of high purity hydrogen. *Int. J. Hydrogen Energy* **2008**, *33*, 5554–5562. [CrossRef]
26. Peña, M.A.; Fierro, J.L.G. Chemical structures and performance of perovskite oxides. *Chem. Rev.* **2001**, *101*, 1981–2018. [CrossRef] [PubMed]
27. Albrecht, K.J.; Jackson, G.S.; Braun, R.J. Thermodynamically consistent modeling of redox-stable perovskite oxides for thermochemical energy conversion and storage. *Appl. Energy* **2016**, *165*, 285–296. [CrossRef]
28. Ishihara, T. (Ed.) *Perovskite Oxide for Solid Oxide Fuel Cells*; Fuel Cells and Hydrogen Energy; Springer US: Boston, MA, USA, 2009; ISBN 978-0-387-77707-8.
29. Emery, A.A.; Saal, J.E.; Kirklin, S.; Hegde, V.I.; Wolverton, C. High-throughput computational screening of perovskites for thermochemical water splitting applications. *Chem. Mater.* **2016**, *28*, 5621–5634. [CrossRef]
30. Yang, C.-K.; Yamazaki, Y.; Aydin, A.; Haile, S.M. Thermodynamic and kinetic assessments of strontium-doped lanthanum manganite perovskites for two-step thermochemical water splitting. *J. Mater. Chem. A* **2014**, *2*, 13612–13623. [CrossRef]
31. Agrafiotis, C.; Roeb, M.; Sattler, C. A review on solar thermal syngas production via redox pair-based water/carbon dioxide splitting thermochemical cycles. *Renew. Sustain. Energy Rev.* **2015**, *42*, 254–285. [CrossRef]
32. Demont, A.; Abanades, S.; Beche, E. Investigation of Perovskite Structures as Oxygen-Exchange Redox Materials for Hydrogen Production from Thermochemical Two-Step Water-Splitting Cycles. *J. Phys. Chem. C* **2014**, *118*, 12682–12692. [CrossRef]
33. Bork, A.H.; Povoden-Karadeniz, E.; Rupp, J.L.M. Modeling Thermochemical Solar-to-Fuel Conversion: CALPHAD for Thermodynamic Assessment Studies of Perovskites, Exemplified for (La,Sr)MnO_3. *Adv. Energy Mater.* **2017**, *7*, 1601086. [CrossRef]
34. Kuo, J.H.; Anderson, H.U.; Sparlin, D.M. Oxidation-reduction behavior of undoped and Sr-doped $LaMnO_3$ nonstoichiometry and defect structure. *J. Solid State Chem.* **1989**, *83*, 52–60. [CrossRef]
35. Mizusaki, J. Oxygen nonstoichiometry and defect equilibrium in the perovskite-type oxides $La_{1-x}Sr_xMnO_{3+d}$. *Solid State Ionics* **2000**, *129*, 163–177. [CrossRef]
36. Dey, S.; Rao, C.N.R. Splitting of CO_2 by Manganite Perovskites to Generate CO by Solar Isothermal Redox Cycling. *ACS Energy Lett.* **2016**, *1*, 237–243. [CrossRef]
37. Demont, A.; Abanades, S. High redox activity of Sr-substituted lanthanum manganite perovskites for two-step thermochemical dissociation of CO_2. *RSC Adv.* **2014**, *4*, 54885–54891. [CrossRef]
38. Nair, M.M.; Abanades, S. Experimental screening of perovskite oxides as efficient redox materials for solar thermochemical CO_2 conversion. *Sustain. Energy Fuels* **2018**. [CrossRef]
39. Gálvez, M.E.; Jacot, R.; Scheffe, J.; Cooper, T.; Patzke, G.; Steinfeld, A. Physico-chemical changes in Ca, Sr and Al-doped La–Mn–O perovskites upon thermochemical splitting of CO_2 via redox cycling. *Phys. Chem. Chem. Phys.* **2015**, *17*, 6629–6634. [CrossRef]
40. Shannon Radii. Available online: http://abulafia.mt.ic.ac.uk/shannon/ptable.php (accessed on 4 January 2018).
41. Demont, A.; Abanades, S. Solar thermochemical conversion of CO_2 into fuel via two-step redox cycling of non-stoichiometric Mn-containing perovskite oxides. *J. Mater. Chem. A* **2015**, *3*, 3536–3546. [CrossRef]
42. Maiti, D.; Hare, B.J.; Daza, Y.A.; Ramos, A.E.; Kuhn, J.N.; Bhethanabotla, V.R. Earth abundant perovskite oxides for low temperature CO_2 conversion. *Energy Environ. Sci.* **2018**, *11*, 648–659. [CrossRef]
43. Wang, L.; Al-Mamun, M.; Liu, P.; Zhong, Y.L.; Wang, Y.; Yang, H.G.; Zhao, H. Enhanced Thermochemical H_2 Production on Ca-Doped Lanthanum Manganite Perovskites Through Optimizing the Dopant Level and Re-oxidation Temperature. *Acta Metall. Sin.* **2018**, *31*, 431–439. [CrossRef]
44. Rao, C.N.R.; Dey, S. Generation of H_2 and CO by solar thermochemical splitting of H_2O and CO_2 by employing metal oxides. *J. Solid State Chem.* **2016**, *242*, 107–115. [CrossRef]
45. Ezbiri, M. Design of Perovskite Redox Materials for the Thermochemical Splitting of H_2O and CO_2 and for O_2 Separation. Ph.D. Thesis, ETH Zurich, Zurich, Switzerland, 2017.
46. Dey, S.; Naidu, B.S.; Rao, C.N.R. $Ln_{0.5}A_{0.5}MnO_3$ (Ln = Lanthanide, A = Ca, Sr) Perovskites Exhibiting Remarkable Performance in the Thermochemical Generation of CO and H_2 from CO_2 and H_2 O. *Chem. A Eur. J.* **2015**, *21*, 7077–7081. [CrossRef] [PubMed]

47. Dey, S.; Naidu, B.S.; Govindaraj, A.; Rao, C.N.R. Noteworthy performance of $La_{1-x}Ca_xMnO_3$ perovskites in generating H_2 and CO by the thermochemical splitting of H_2O and CO_2. *Phys. Chem. Chem. Phys.* **2015**, *17*, 122–125. [CrossRef] [PubMed]
48. Rao, C.N.R.; Dey, S. Solar thermochemical splitting of water to generate hydrogen. *Proc. Natl. Acad. Sci. USA* **2017**, *114*, 13385–13393. [CrossRef] [PubMed]
49. Nair, M.M.; Abanades, S. Insights into the Redox Performance of Non-stoichiometric Lanthanum Manganite Perovskites for Solar Thermochemical CO_2 Splitting. *ChemistrySelect* **2016**, *1*, 4449–4457. [CrossRef]
50. Cooper, T.; Scheffe, J.R.; Galvez, M.E.; Jacot, R.; Patzke, G.; Steinfeld, A. Lanthanum Manganite Perovskites with Ca/Sr A-site and Al B-site Doping as Effective Oxygen Exchange Materials for Solar Thermochemical Fuel Production. *Energy Technol.* **2015**, *3*, 1130–1142. [CrossRef]
51. McDaniel, A.H.; Miller, E.C.; Arifin, D.; Ambrosini, A.; Coker, E.N.; O'Hayre, R.; Chueh, W.C.; Tong, J. Sr- and Mn-doped $LaAlO_{3-\delta}$ for solar thermochemical H_2 and CO production. *Energy Environ. Sci.* **2013**, *6*, 2424–2428. [CrossRef]
52. Miller, J.E.; Ambrosini, A.; Coker, E.N.; Allendorf, M.D.; McDaniel, A.H. Advancing Oxide Materials for Thermochemical Production of Solar Fuels. *Energy Procedia* **2014**, *49*, 2019–2026. [CrossRef]
53. Sastre, D.; Carrillo, A.J.; Serrano, D.P.; Pizarro, P.; Coronado, J.M. Exploring the Redox Behavior of $La_{0.6}Sr_{0.4}Mn_{1-x}Al_xO_3$ Perovskites for CO_2-Splitting in Thermochemical Cycles. *Top. Catal.* **2017**, *60*, 1108–1118. [CrossRef]
54. Cimino, S.; Lisi, L.; De Rossi, S.; Faticanti, M.; Porta, P. Methane combustion and CO oxidation on $LaAl_{1-x}Mn_xO_3$ perovskite-type oxide solid solutions. *Appl. Catal. B Environ.* **2003**, *43*, 397–406. [CrossRef]
55. Ezbiri, M.; Takacs, M.; Theiler, D.; Michalsky, R.; Steinfeld, A. Tunable thermodynamic activity of $La_xSr_{1-x}Mn_yAl_{1-y}O_{3-\delta}$ ($0 \leq x \leq 1$, $0 \leq y \leq 1$) perovskites for solar thermochemical fuel synthesis. *J. Mater. Chem. A* **2017**, *5*, 4172–4182. [CrossRef] [PubMed]
56. Deml, A.M.; Stevanović, V.; Holder, A.M.; Sanders, M.; O'Hayre, R.; Musgrave, C.B. Tunable Oxygen Vacancy Formation Energetics in the Complex Perovskite Oxide $Sr_xLa_{1-x}Mn_yAl_{1-y}O_3$. *Chem. Mater.* **2014**, *26*, 6595–6602. [CrossRef]
57. Sugiyama, Y.; Gokon, N.I.; Cho, H.-S.; Bellan, S.; Hatamachi, T.; Kodama, T. Thermochemical two-step water-splitting using perovskite oxide for solar hydrogen production. In *Asian Conference on Thermal Sciences 2017*; ICC Jeju: Jeju Island, Korea, 2017.
58. Wang, L.; Al-Mamun, M.; Liu, P.; Wang, Y.; Yang, H.G.; Zhao, H. $La_{1-x}Ca_xMn_{1-y}Al_yO_3$ perovskites as efficient catalysts for two-step thermochemical water splitting in conjunction with exceptional hydrogen yields. *Chin. J. Catal.* **2017**, *38*, 1079–1086. [CrossRef]
59. Wang, L.; Al-Mamun, M.; Zhong, Y.L.; Jiang, L.; Liu, P.; Wang, Y.; Yang, H.G.; Zhao, H. Ca^{2+} and Ga^{3+} doped $LaMnO_3$ perovskite as a highly efficient and stable catalyst for two-step thermochemical water splitting. *Sustain. Energy Fuels* **2017**, *1*, 1013–1017. [CrossRef]
60. Dey, S.; Naidu, B.S.; Rao, C.N.R. Beneficial effects of substituting trivalent ions in the B-site of $La_{0.5}Sr_{0.5}Mn_{1-x}A_xO_3$ (A = Al, Ga, Sc) on the thermochemical generation of CO and H_2 from CO_2 and H_2O. *Dalton Trans.* **2016**, *45*, 2430–2435. [CrossRef] [PubMed]
61. Luciani, G.; Landi, G.; Aronne, A.; Di Benedetto, A. Partial substitution of B cation in $La_{0.6}Sr_{0.4}MnO_3$ perovskites: A promising strategy to improve the redox properties useful for solar thermochemical water and carbon dioxide splitting. *Solar Energy* **2018**, *171*, 1–7. [CrossRef]
62. Wang, L.; Al-Mamun, M.; Liu, P.; Wang, Y.; Yang, H.G.; Zhao, H. Notable hydrogen production on $La_xCa_{1-x}CoO_3$ perovskites via two-step thermochemical water splitting. *J. Mater. Sci.* **2018**, *53*, 6796–6806. [CrossRef]
63. Orfila, M.; Linares, M.; Molina, R.; Botas, J.Á.; Sanz, R.; Marugán, J. Perovskite materials for hydrogen production by thermochemical water splitting. *Int. J. Hydrogen Energy* **2016**, *41*, 19329–19338. [CrossRef]
64. Wang, L.; Al-Mamun, M.; Zhong, Y.L.; Liu, P.; Wang, Y.; Yang, H.G.; Zhao, H. Enhanced Thermochemical Water Splitting through Formation of Oxygen Vacancy in $La_{0.6}Sr_{0.4}BO_{3-\delta}$ (B=Cr, Mn, Fe, Co, and Ni) Perovskites. *ChemPlusChem* **2018**. [CrossRef]
65. Bork, A.H.; Kubicek, M.; Struzik, M.; Rupp, J.L.M. Perovskite $La_{0.6}Sr_{0.4}Cr_{1-x}Co_xO_{3-\delta}$ solid solutions for solar-thermochemical fuel production: Strategies to lower the operation temperature. *J. Mater. Chem. A* **2015**, *3*, 15546–15557. [CrossRef]

66. Rodenbough, P.P.; Chan, S.-W. Thermal oxygen exchange cycles in mixed manganese perovskites. *Ceram. Int.* **2018**, *44*, 1343–1347. [CrossRef]
67. Barcellos, D.R.; Sanders, M.D.; Tong, J.; McDaniel, A.H.; O'Hayre, R.P. $BaCe_{0.25}Mn_{0.75}O_{3-\delta}$—A promising perovskite-type oxide for solar thermochemical hydrogen production. *Energy Environ. Sci.* **2018**. [CrossRef]
68. Vyazovkin, S.; Burnham, A.K.; Criado, J.M.; Pérez-Maqueda, L.A.; Popescu, C.; Sbirrazzuoli, N. ICTAC Kinetics Committee recommendations for performing kinetic computations on thermal analysis data. *Thermochim. Acta* **2011**, *520*, 1–19. [CrossRef]
69. Khawam, A.; Flanagan, D.R. Solid-State Kinetic Models: Basics and Mathematical Fundamentals. *The J. Phys. Chem. B* **2006**, *110*, 17315–17328. [CrossRef]
70. Jiang, Q.; Tong, J.; Zhou, G.; Jiang, Z.; Li, Z.; Li, C. Thermochemical CO_2 splitting reaction with supported $La_xA_{1-x}Fe_yB_{1-y}O_3$ (A=Sr, Ce, B=Co, Mn; $0 \leq x, y \leq 1$) perovskite oxides. *Sol. Energy* **2014**, *103*, 425–437. [CrossRef]
71. Gotor, F.J.; Criado, J.M.; Malek, J.; Koga, N. Kinetic Analysis of Solid-State Reactions: The Universality of Master Plots for Analyzing Isothermal and Nonisothermal Experiments. *J. Phys. Chem. A* **2000**, *104*, 10777–10782. [CrossRef]
72. Criado, J.M.; Pérez-Maqueda, L.A.; Gotor, F.J.; Málek, J.; Koga, N. A unified theory for the kinetic analysis of solid state reactions under any thermal pathway. *J. Therm. Anal. Calorim.* **2003**, *72*, 901–906. [CrossRef]
73. McDaniel, A.H.; Ambrosini, A.; Coker, E.N.; Miller, J.E.; Chueh, W.C.; O'Hayre, R.; Tong, J. Nonstoichiometric Perovskite Oxides for Solar Thermochemical H_2 and CO Production. *Energy Procedia* **2014**, *49*, 2009–2018. [CrossRef]
74. Scheffe, J.R.; McDaniel, A.H.; Allendorf, M.D.; Weimer, A.W. Kinetics and mechanism of solar-thermochemical H_2 production by oxidation of a cobalt ferrite–zirconia composite. *Energy Environ. Sci.* **2013**, *6*, 963. [CrossRef]
75. Arifin, D.; Weimer, A.W. Kinetics and mechanism of solar-thermochemical H_2 and CO production by oxidation of reduced CeO_2. *Sol. Energy* **2018**, *160*, 178–185. [CrossRef]
76. Kim, Y.; Jeong, S.J.; Koo, B.; Lee, S.; Kwak, N.W.; Jung, W. Study of the surface reaction kinetics of (La,Sr)$MnO_{3-\delta}$ oxygen carriers for solar thermochemical fuel production. *J. Mater. Chem. A* **2018**, *6*, 13082–13089. [CrossRef]
77. Davenport, T.C.; Yang, C.-K.; Kucharczyk, C.J.; Ignatowich, M.J.; Haile, S.M. Maximizing fuel production rates in isothermal solar thermochemical fuel production. *Appl. Energy* **2016**, *183*, 1098–1111. [CrossRef]
78. Davenport, T.C.; Yang, C.-K.; Kucharczyk, C.J.; Ignatowich, M.J.; Haile, S.M. Implications of Exceptional Material Kinetics on Thermochemical Fuel Production Rates. *Energy Technol.* **2016**, *4*, 764–770. [CrossRef]